Electrochimica Acta 321 (2019) 134648

Contents lists available at ScienceDirect

Electrochimica Acta

journal homepage: www.elsevier.com/locate/electacta

Theoretical validation of the step potential electrochemical spectroscopy (SPECS) and multiple potential step chronoamperometry (MUSCA) methods for pseudocapacitive electrodes

Obaidallah Munteshari [a, b], Yucheng Zhou [a], Bing-Ang Mei [a, c], Laurent Pilon [a, d, *]

[a] Mechanical and Aerospace Engineering Department, Henry Samueli School of Engineering and Applied Science, University of California, Los Angeles, CA, 90095, USA
[b] Mechanical Engineering Department, King Fahd University of Petroleum and Minerals (KFUPM), Dhahran 31261, Saudi Arabia
[c] School of Mechanical Engineering, Beijing Institute of Technology, Beijing, 100081, China
[d] California NanoSystems Institute, University of California, Los Angeles, CA90095, USA

ARTICLE INFO

Article history:
Received 23 May 2019
Received in revised form
16 July 2019
Accepted 6 August 2019
Available online 9 August 2019

Keywords:
Pseudocapacitive electrode
Electrochemical methods
Potential step chronoamperometry

ABSTRACT

This study theoretically and rigorously validates the use of the recently proposed step potential electrochemical spectroscopy (SPECS) and multiple potential step chronoamperometry (MUSCA) methods and their fitting analysis for determining the respective contributions of electrical double layer (EDL) and faradaic reactions to charge storage in pseudocapacitive electrodes. The continuum modified Poisson-Nernst-Planck model coupled with the Frumkin-Butler-Volmer theory were used for simulating interfacial, transport, and electrochemical phenomena in pseudocapacitive electrodes. The model accounted for (i) electron transport in the electrode, (ii) reversible redox reactions, (iii) ion electrodiffusion in binary and symmetric electrolytes, (iv) ion intercalation into the pseudocapacitive electrode, and (v) steric repulsion due to finite ion size. First, typical experimental measurements obtained from the SPECS method were reproduced numerically for a planar pseudocapacitive electrode. The EDL and faradaic currents retrieved from the SPECS fitting procedure were found to be in excellent agreement with those defined from first principles and computed numerically. Here, the faradaic current was modeled in the SPECS method as a diffusion process accounting for interfacial charge transfer kinetics and IR drop. The resistance obtained by SPECS matched the internal resistance obtained from electrochemical impedance spectroscopy. Similarly, the EDL capacitance retrieved by SPECS corresponded to the differential capacitance obtained from cyclic voltammetry (CV). Finally, the CV curves were successfully corrected for ohmic polarization effect using the MUSCA method. Then, the capacitive and diffusive currents retrieved from the electrochemical analysis of CV curves corrected by the MUSCA method were in good agreement with the EDL and faradaic currents reconstructed from the MUSCA method.

© 2019 Elsevier Ltd. All rights reserved.

1. Introduction

Electrochemical capacitors (ECs) differ from batteries by their high power density, long cycle life, and high cycle efficiency [1]. Depending on their charging mechanism, EC electrodes can be classified as electrical double layer (EDL) and pseudocapacitive electrodes [1,2]. EDL electrodes are typically made of carbon-based materials, with large specific surface area, immersed in an electrolyte. They store charge physically via electrical double layer formation as ions accumulate at the electrode/electrolyte interface [1,2]. On the other hand, pseudocapacitive electrodes store charges chemically via reduction/oxidation (redox) reactions at the electrode surface in addition to EDL formation [2,3]. These redox reactions may be accompanied by ion intercalation/deintercalation in/out of the electrode. Transition metal oxides (e.g., Nb_2O_5, MnO_2, MoO_2, MoS_2) have been considered as pseudocapacitive electrode materials due to their high theoretical capacity, chemical stability, and high redox reaction reversibility [4–6].

Several electrochemical techniques are typically used to characterize EC electrodes including cyclic voltammetry (CV),

---

* Corresponding author. Mechanical and Aerospace Engineering Department, Henry Samueli School of Engineering and Applied Science, University of California, Los Angeles, CA, 90095, USA.

E-mail address: pilon@seas.ucla.edu (L. Pilon).

https://doi.org/10.1016/j.electacta.2019.134648
0013-4686/© 2019 Elsevier Ltd. All rights reserved.

Nomenclature

a	Effective ion diameter (nm)
c	Ion concentration (mol L^{-1})
$c_{1,P}$	Concentration of ion in the electrode (mol L^{-1})
$c_{1,P,0}$	Initial concentration of ion in the electrode (mol L^{-1})
$c_{1,P,max}$	Maximum concentration of intercalated ion (mol L^{-1})
C_{EDL}	EDL capacitance (μF cm^{-2})
$C_{diff,i}$	Differential capacitance (μF cm^{-2})
C_{int}	Integral capacitance (μF cm^{-2})
D	Diffusion coefficient of ions in electrolyte (m^2 s^{-1})
$D_{1,P}$	Diffusion coefficient of ion in the electrode (m^2 s^{-1})
e	Elementary charge, $e = 1.602 \times 10^{-19}$ C
f	Frequency (Hz)
F	Faraday's constant, $F = eN_A = 9.648 \times 10^4$ C mol^{-1}
H	Stern layer thickness (nm)
i	Imaginary unit, $i^2 = -1$
j	Current density (A m^{-2})
$j_{F,0}$	Exchange current density due to faradaic reactions (A m^{-2})
k_0	Reaction rate constant ($m^{2.5}mol^{-0.5}s^{-1}$)
k_B	Boltzmann constant, $k_B = 1.38 \times 10^{-23}$ m^2 kg s^{-2} K^{-1}
L	Total thickness of the electrolyte domain (nm)
L_D	Thickness of the diffuse layer (nm)
L_P	Total thickness of the pseudocapacitive electrode (nm)
n_c	Cycle number
N_A	Avogadro number, $N_A = 6.022 \times 10^{23}$ mol^{-1}
N_i	Ion flux of species i (mol $m^{-2}s^{-1}$)
p_s	Step number
ΔQ_F	Total amount of charges stored due to the faradaic current (C)
R_{ct}	Charge transfer resistance (Ω m^2)
R_{EDL}	EDL resistance (Ω m^2)
R_s	Internal resistance (Ω m^2)
R_d	diffuse resistance (Ω m^2)
R_∞	Bulk electrolyte resistance (Ω m^2)
R_u	Universal gas constant, $R_u = 8.314$ J $mol^{-1}K^{-1}$
T	Local temperature (K)
t	Time (s)
t_e	Equilibration time (s)
t_t	Transition time (s)
t_{cd}	Charging discharging cycle period (s)
Δt	Time step (data acquisition time) (s)
z	Ion valency
Z	Impedance, $Z = Z_{re} + iZ_{im}$ (Ω m^2 or Ω)
Z_{re}, Z_{im}	Real and imaginary parts of the impedance (Ω m^2 or Ω)

Greek symbols

α	Transfer coefficient
ε_0	Vacuum permittivity, $\varepsilon_0 = 8.854 \times 10^{-12}$ F m^{-1}
ε_r	Relative permittivity of the electrolyte
η	Overpotential (V)
ν	Scan rate for cyclic voltammetry (V s^{-1})
σ	Electrical conductivity (S m^{-1})
τ_d	Diffusion time constant (s)
ψ	Electric potential (V)
$\psi_{s,min}$, $\psi_{s,max}$	Minimum and maximum of the potential window (V)
$\Delta\psi_s$	Potential step (V)
$\Delta\psi_{eq}$	Equilibrium potential difference (V)

Superscripts and subscripts

∞	Refers to bulk electrolyte
0	Refers to the amplitude of oscillations
C	Refers to the capacitive component
D	Refers to diffuse component
EDL	Refers to electrical double layer component
dc	Refers to the time-independent DC component
F	Refers to the faradaic component
H	Refers to Stern layer
i	Refers to ion species i
M	Refers to the MUSCA method
s	Refers to electrode/current collector interface
S	Refers to the SPECS method

galvanostatic cycling (GC), and electrochemical impedance spectroscopy (EIS) [7]. Several studies have shown that these techniques provide the same value of supercapacitor metrics [7–13]. For example, the internal resistance retrieved from IR drop was numerically and experimentally found to be equaled to that obtained by EIS [8,9,11]. In addition, the differential capacitance $\boldsymbol{C_{diff}}$ at a given potential can be obtained from CV, GC, and EIS measurements [7,10,12,13]. However, one of the main challenges in characterizing pseudocapacitive electrodes is to discriminate the contributions from faradaic reactions and EDL formation. To do so, several empirical and physical models have been developed to analyze CV measurements including the so-called k_1, k_2 analysis [14,15]. More recently, step potential electrochemical spectroscopy (SPECS) method has been proposed to differentiate the contribution of faradaic current $j_F(t)$ from that of EDL current $j_{EDL}(t)$ to the total current in pseudocapacitive electrodes [16–18]. Moreover, Shao et al. [19] have developed a new electrochemical method termed multiple potential step chronoamperometry (MUSCA) to minimize the ohmic polarization effect in CV curves. Then, the k_1, k_2 analysis was applied on the corrected CV curves [19].

This study aims to theoretically validate the use of the SPECS and MUSCA methods and their corresponding analysis for distinguishing the respective contributions of faradaic reactions and electrical double layer to charge storage in pseudocapacitive electrodes. To do so, detailed numerical simulations were performed for a pseudocapacitive planar electrode in three-electrode configuration using a continuum model based on first-principles and predicting the spatiotemporal evolution of the electric potential and ion concentrations in the electrode and electrolyte [20].

2. Background

2.1. $\boldsymbol{k_1}, \boldsymbol{k_2}$ analysis

The *ad hoc* semiempirical model known as k_1, k_2 analysis has been used extensively to analyze CV curves at relatively low scan rates to characterize the contribution from capacitive and diffusion currents to the total current measured in pseudocapacitive electrodes [14,15]. It has recently been validated theoretically from numerical simulations of pseudocapacitive electrodes consisting of a cylindrical rod scaffold coated with a redox active layer [21]. The k_1, k_2 analysis is based on the facts that, at a given potential ψ_s, (i) the capacitive current density $j_C(\psi_s)$ is due to either EDL formation and/or fast redox reactions and (ii) the diffusional current density $j_D(\psi_s)$ is due to diffusion-controlled process in semi-infinite solid, such as redox reactions involving slow ion intercalation/deintercalation [14]. This model assumes that the total current density $j_T(\psi_s)$ is the summation of (i) the capacitive current density $j_C(\psi_s)$ linearly proportional to scan rate ν and (ii) diffusion current density $j_D(\psi_s)$ proportional to the square root of scan rate ν such that [14],

$$j_T(\psi_s) = j_C(\psi_s) + j_D(\psi_s) = k_1(\psi_s)\,\nu + k_2(\psi_s)\,\nu^{1/2}. \tag{1}$$

Here, $k_1(\psi_s)$ and $k_2(\psi_s)$ are semi-empirical functions dependent only on the electrode potential ψ_s. They can be found by rewriting Equation (1) according to Ref. [14],

$$\frac{j_T(\psi_s)}{\nu^{1/2}} = k_1(\psi_s)\,\nu^{1/2} + k_2(\psi_s) \tag{2}$$

where $k_1(\psi_s)$ and $k_2(\psi_s)$ correspond respectively to the slope and the intercept of the plot of $j_T(\psi_s)/\nu^{1/2}$ versus $\nu^{1/2}$ at a given potential ψ_s. Here, the term “capacitive current” used to designate $j_C(\psi_s)$ may be misleading since it is not limited to EDL formation but also includes fast redox reactions with or without intercalation/deintercalation [15]. In other words, this analysis does not explicitly distinguish the contribution from redox reactions and from EDL formation.

2.2. SPECS

The recently proposed step potential electrochemical spectroscopy (SPECS) method [16–18] consists of imposing a series of small potential steps $\Delta\psi_s$ within a potential window ranging between $\psi_{s,min}$ and $\psi_{s,max}$. The current response is recorded as a function of time for each potential step. This method has also been called potential step chronoamperometry and used as a way to evaluate the contribution of EDL formation and faradaic reactions to charge storage [16–18]. Dupont and Donne [16–18] suggested that the total current response $j_T^S(t)$ to an applied potential step across a pseudocapacitive electrode can be treated as the superposition of an EDL current $j_{EDL}^S(t)$, a faradaic current $j_F^S(t)$, and a residual current $j_r^S(t)$ according to [16–18],

$$j_T^S(t) = j_{EDL}^S(t) + j_F^S(t) + j_r^S(t). \tag{3}$$

Here, $j_{EDL}^S(t)$ was described by the current response of an equivalent resistance-capacitor (RC) circuit model. The simplest form of RC circuit consists of an equivalent resistance R_{EDL} (in Ω m^2) in series with an ideal electrical double layer capacitor C_{EDL} (in F m^{-2}) [7]. Then, the current j_{EDL}^S (in A m^{-2}) associated with EDL formation in response to applying a potential step $\Delta\psi_s$ can be expressed as [7],

$$j_{EDL}^S(t) = \frac{\Delta\psi_s}{R_{EDL}}\exp\left(-\frac{t}{\tau_{EDL}}\right) \tag{4}$$

where $\tau_{EDL} = R_{EDL}C_{EDL}$ is the time constant of EDL formation. The authors further suggested that the EDL current was due to the EDL formation (i) at the geometric surface of the electrode (equivalent to EDL formation on a planar electrode) and (ii) within micropores and mesopores [16–18]. These two terms were both modeled as a resistor and capacitor in series and had the same form as Equation (4) but different fitting parameters.

Moreover, the response of faradaic current density $j_F^S(t)$ (in A m^{-2}) to an imposed potential step as a function of time t has been modeled using the Cottrell relationship for semi-infinite diffusion process in a planar electrode given by [7],

$$j_F^S(t) = Bt^{-1/2} = \frac{\Delta Q_F}{\sqrt{\pi\tau_d}}t^{-1/2}. \tag{5}$$

where ΔQ_F and τ_d are respectively the total amount of charges stored due to the faradaic current and the diffusion time constant expressed as [22,23],

$$\Delta Q_F = \int_t^{t+\Delta t} j_F^S \mathrm{d}t = -FL_d\Delta c_{1,P} \quad \text{and} \quad \tau_d = \frac{L_d^2}{D_d}. \tag{6}$$

Here, $F = eN_A = 9.648 \times 10^4$ C mol^{-1} is the Faraday's constant, D_d is the diffusion coefficient of intercalated ion species (Li$^+$) in the pseudocapacitive electrode, L_d is the diffusion length, and $\Delta c_{1,P}$ is the net change in intercalated ion concentration in the pseudocapacitive electrode caused by the applied step potential $\Delta\psi_s$ between two consecutive steps, i.e., $\Delta c_{1,P} = c_{1,P}(\psi_s + \Delta\psi_s) - c_{1,P}(\psi_s)$. The Cottrell relationship has been used in several studies to deconvolute the contribution of EDL and faradaic currents using the SPECS method [24–27]. However, Montella [23] has shown that Equation (5) is only valid for estimating $j_F^S(t)$ for short times, i.e., $t \ll \tau_d$.

Alternatively, the faradaic current $j_F(t)$ can be derived based on Fick's second law of diffusion for long time range ($t \gg \tau_d$) under finite-space conditions as [17,22,23,28],

$$j_F^S(t) = 2\frac{\Delta Q_F}{\tau_d}\sum_{n=1}^{\infty}\exp\left[-(2n-1)^2\frac{\pi^2 t}{4\tau_d}\right]. \tag{7}$$

However, this model ignores the IR drop and EDL formation at the electrode surface and assumes that the insertion process is solely diffusion-controlled. Montella [23] formulated a model for the current response of ion intercalation/deintercalation in a redox active planar electrode subjected to a potential step $\Delta\psi_s$. This model accounts for the interfacial charge transfer kinetics process and the effect of IR drop and EDL formation on the faradaic current density according to,

$$j_F^S(t) = 2\frac{\Delta Q_F}{\tau_d}\sum_{n=1}^{\infty}\frac{\Lambda^2}{\Lambda^2 + \Lambda + b_n^2}\exp\left(-\frac{b_n^2 t}{\tau_d}\right) \tag{8}$$

where b_n is the n^{th} root of the following equation [23].

$$b_n \tan b_n - \Lambda = 0. \tag{9}$$

Here, Λ is a dimensionless resistance expressed as [23],

$$\Lambda = \frac{R_d}{R_s + R_{ct}} \tag{10}$$

where R_d, R_s, and R_{ct} are the diffusion, internal, and interfacial charge transfer resistances, respectively. The value of Λ characterizes the charge storage mechanism. For diffusion controlled processes, $R_d \gg R_s + R_{ct}$ and the value of Λ is very large such that $b_1 = \pi/2$ [23]. In this case, Equation (8) reduces to the first term of the summation in Equation (7). On the other hand, when processes are controlled by fast interfacial charge transfer kinetics and/or ohmic drop $\Lambda \ll 1$ and $b_1 \simeq \sqrt{\Lambda}$ [23]. Finally, intermediate values of Λ is characteristic of processes controlled by both solid state diffusion and interfacial charge transfer kinetics [23]. This model has been used successfully in combination with potentiostatic intermittent titration technique (PITT) to estimate Li$^+$ diffusion coefficient in amorphous TiO_x nanotubes [29]. However, it has never been used in combination with the SPECS method for pseudocapacitive electrodes.

Finally, j_r^S was considered as a constant term to account for the leakage current and/or residual current associated with electrolyte decomposition reactions and/or parasitic reactions in the electrode material [16–18].

2.3. MUSCA

The conventional CV measurements suffer from ohmic polarization, especially at high scan rate [19]. The MUSCA method aims to correct for the drift of the redox peaks with increasing scan rate observed in cyclic voltammetry by minimizing the effect of parasitic redox reactions (residual current) and ohmic polarization [19]. Thus, the MUSCA method is carried out by imposing a series of potential steps of $\Delta\psi_s$ across a given potential window ($\psi_{s,min} - \psi_{s,max}$) and measuring the current response for each step by allowing the current density to decay to zero under equilibrium conditions before applying the next step. It is similar to SPECS in the electrochemical measurements but differs from SPECS in the data analysis method. In order to reconstruct CV curves at scan rate ν using the MUSCA method, the current measured in SPECS is averaged over a certain time t_ν defined from the beginning of the potential step to determine the mean current j_i^M at potential ψ_s such that [19],

$$j_i^M(\psi_s)=\frac{1}{t_\nu}\int_0^{t_\nu} j_i(t)\,\mathrm{d}t \quad \text{with} \ \ i=T,\ EDL,\ \text{or}\ F \tag{11}$$

where the superscript "*M*" refers to the MUSCA method and t_ν is chosen based on the desired scan rate ν according to [19],

$$t_\nu=\frac{\Delta\psi_s}{\nu}. \tag{12}$$

Afterward, the CV curves are reconstructed from the MUSCA measurements by plotting j_T^M vs. ψ_s [19]. Finally, the reconstructed CV curves can then be used to characterize the electrochemical behavior of pseudocapacitive electrodes using the k_1, k_2 analysis previously described to "separate better diffusion from capacitive currents" [19]. Note that the MUSCA method has not been used explicitly to identify the EDL and faradaic contributions to the total current.

3. Analysis

3.1. Schematic and assumptions

Fig. 1 shows the coordinate system and dimensions of our simulated domain consisting of a planar pseudocapacitive electrode supported by a planar current collector in an electrolyte containing Li^+ ions in a three-electrode configuration. The pseudocapacitive electrode and electrolyte thicknesses were denoted by L_P and L, respectively.

To make the problem mathematically tractable, the following assumptions were made: (1) the electrolyte was binary and symmetric, i.e., it consisted of two ion species of opposite valency $\pm z$. (2) Cations and anions had the same diffusion coefficient D and effective diameter a [30,31]. (3) The Stern layer contained no free charge and its thickness H was approximated as the radius of the ions so that $H = a/2$ [7,32,33]. (4) The transport properties of the electrode and electrolyte were taken as constant and independent of state-of-charge. (5) Bulk motion of the electrolyte was negligible. (6) Ion intercalation in the electrode was modeled as a diffusion process. (7) Heat generation was ignored and the temperature T was uniform and constant in the electrode and electrolyte. (8) The contact resistance between the electrode and the current collector and the resistance of the current collector were negligible. (9) Self-discharge and residual current associated with electrolyte decomposition reactions and/or parasitic reactions in the electrode material were ignored, i.e., $j_r = 0$.

The modified Poisson-Nernst-Planck (MPNP) model coupled with the Frumkin-Bulter-Volmer theory were used to numerically reproduce the SPECS method accounting for interfacial, transport, and electrochemical phenomena in the pseudocapacitive electrode [20,34]. The governing equations, initial and boundary conditions, and method of solution were described in detail elsewhere [9,20,35] and need not be repeated. The governing equations were reproduced in Section S.1 for the sake of completeness. In brief, the spatiotemporal evolution of (i) the potential $\psi(x,t)$ in the pseudocapacitive electrode and in the electrolyte and (ii) the concentrations $c_1(x,t)$ of cations and $c_2(x,t)$ of anions in the electrolyte were governed by the MPNP model [Equations (S.1) to (S.3)]. The molar concentration $c_{1,P}(x,t)$ of intercalated cations in the pseudocapacitive electrode was governed by the mass diffusion equation [Equation (S.4)] [35].

3.2. Boundary conditions

All initial and boundary conditions necessary to solve the 1D transient governing equations were reported in Section S.2. The imposed potential $\psi_s(t)$ at the current collector/electrode interface ($x = 0$) was imposed as a multi-step function for SPECS simulations such that,

$$\psi_s(t)=\psi(0,t)=\begin{cases}\psi_{s,min}+p_s\Delta\psi_s & \text{for } 0\le p_s\le (n_s+1)/2\\ \psi_{s,max}-\left(p_s-\dfrac{n_s+1}{2}\right)\Delta\psi_s & \text{for } \ (n_s+1)/2\le p_s\le n_s\end{cases} \tag{13}$$

where $\psi_{s,min}$ and $\psi_{s,max}$ are, respectively, the minimum and maximum potentials and p_s is the step number with n_s is an odd integer corresponding to the total number of potential steps across the potential window between $\psi_{s,min}$ and $\psi_{s,max}$, i.e., $n_s = [2(\psi_{s,max} - \psi_{s,min})/\Delta\psi_s] + 1$. Here, $\psi_s(t)$ is a function of time t where $(p_s - 1)t_e \le t < p_s t_e$ for each potential step and t_e is the equilibration time or the period of each step.

Similarly, a harmonic function of time t was imposed at the current collector/electrode interface ($x = 0$) for EIS simulations such that [7],

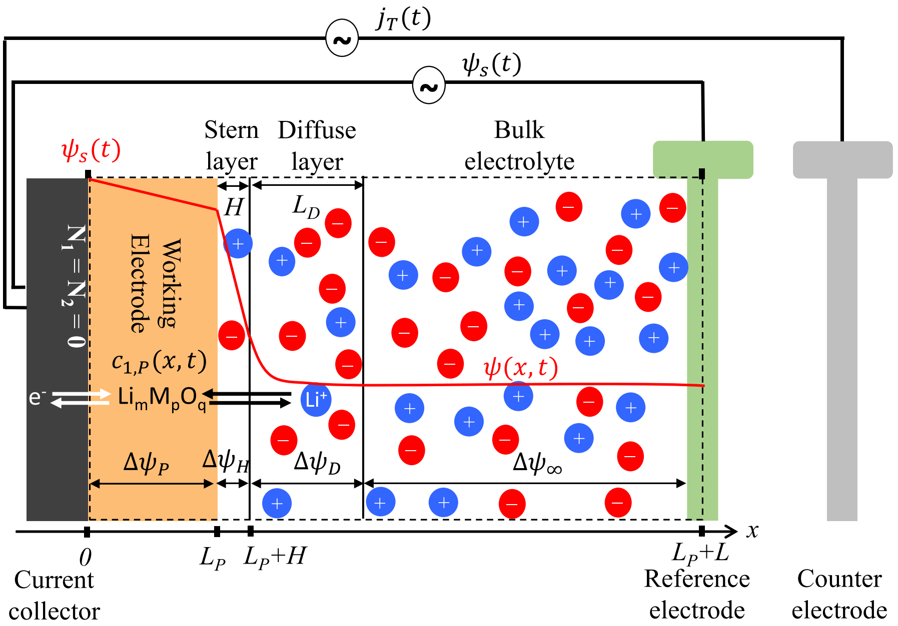

Fig. 1. Schematic, coordinate system, and dimensions of the simulated planar pseudocapacitive electrode in a three-electrode configuration. The dashed line encloses the computational domain simulated.

$$\psi_s(t) = \psi_{dc} + \psi_0 e^{i2\pi ft} \tag{14}$$

where ψ_{dc} is the time-independent DC potential and ψ_0 is the amplitude of the oscillating potential at frequency f.

Finally, the potential $\psi_s(t)$ imposed at the current collector/electrode interface ($x = 0$) was expressed as a triangular function of

$$\psi_s(t) = \begin{cases} \psi_{s,min} + v\left[t - (n_c - 1)t_{cd}\right] & \text{for}(n_c - 1)t_{cd} \le t < (n_c - 1/2)t_{cd} \\ \psi_{s,max} - v\left[t - (n_c - 1/2)t_{cd}\right] & \text{for}(n_c - 1/2)t_{cd} \le t < n_c\, t_{cd} \end{cases} \tag{15}$$

time t for cyclic voltammetry simulations according to [32], where n_c is the cycle number (integer) and t_{cd} is the cycle period.

3.3. Constitutive relationships

The present study uses realistic material properties taken from the literature for the electrolyte [36,37] and the pseudocapacitive electrode [7,38–40]. Table 1 summarizes (i) the electrode thickness L_P and properties including its electrical conductivity σ_P, reaction rate constant k_0, maximum $c_{1,P,max}$ and initial $c_{1,P,0}$ Li$^+$ ion concentrations, transfer coefficient α, and Li$^+$ diffusion coefficient $D_{1,P}$, (ii) the electrolyte thickness L and properties including the bulk ion

Table 1
Value or range of electrode and electrolyte properties and dimensions used in the simulations reported in this study.

Parameter	Symbol	Value	Unit
Ion diameter	a	0.67	nm
Bulk ion concentration	c_∞	1	mol L^{-1}
Maximum ion concentration in the electrode	$c_{1,P,max}$	31.9	mol L^{-1}
Diffusion coefficient in the electrolyte	D	2×10^{-11}	m^2 s^{-1}
Diffusion coefficient in the electrode	$D_{1,P}$	10–^{14}	m^2 s^{-1}
Reaction rate constant	k_0	10^{-9}	m$^{1+3\alpha}$mol$^{-\alpha}$s^{-1}
Electrolyte thickness	L	8	μm
Electrode thickness	L_P	20	nm
Temperature	T	298	K
Valency	z	1	
Transfer coefficient	α	0.5	
Relative permittivity	ε_r	64.4	
Electrode conductivity	σ_P	10^{-4}	S m^{-1}
Potential window	$\psi_{s,min}$	−0.05	V
	$\psi_{s,max}$	0.85	V

concentration c_∞, valency z, relative permittivity ε_r, ion diameter a, and ion diffusion coefficient D, and (iii) the operating conditions including the potential window $\psi_{s,min} - \psi_{s,max}$ and the temperature T (in K).

For electrodes consisting of transition metal oxides, the equilibrium potential difference $\Delta\psi_{eq}$ is typically determined experimentally as a function of the state-of-charge (SOC) defined as $c_{1,P}/c_{1,P,max}$ by fitting experimental data for open-circuit potential [41–43]. For the sake of simplicity, $\Delta\psi_{eq}$ was modeled as a linear function of SOC as measured for 100 μm thick MnO_2 dense films [39],

$$\Delta\psi_{eq}(t) = 10.5\left[4 - c_{1,P}(t)/c_{1,P,max}\right] - 39.9. \tag{16}$$

Here, $c_{1,P,max}$ was taken as $c_{1,P,max} \approx 31.9$ mol L^{-1} corresponding to fully lithiated manganese dioxide $LiMnO_2$ [21,40]. The transfer coefficient α was assumed to be 0.5 to consider the ideal case of identical energy barriers for forward and backward reversible redox reactions [7]. The diffusion coefficient $D_{1,P}$ of the intercalated Li^+ in the transition metal oxides typically ranges from 10^{-16} to 10^{-10} m^2 s^{-1} [38]. Here, $D_{1,P}$ was arbitrary chosen as 10^{-14} m^2 s^{-1}.

As for the electrolyte, we considered 1 M $LiClO_4$ salt in propylene carbonate (PC) solvent such that the bulk ion concentration $c_\infty = 1$ mol L^{-1} and valency $z = 1$. The relative permittivity was taken as a constant equal to that of PC, i.e., $\varepsilon_r = 64.4$ [37]. The effective solvated ion diameter a and the ion diffusion coefficient D were taken as those of solvated Li^+ ions in PC such that $a = 0.67$ nm and $D = 2\times 10^{-11}$ m^2 s^{-1} [36].

3.4. Data processing

The total current density at the electrode/electrolyte interface $j_T(t)$ can be expressed as the sum of (i) the EDL current density $j_{EDL}(t)$ and (ii) the faradaic current density $j_F(t)$, i.e., $j_T(t) = j_{EDL}(t) + j_F(t)$. On the one hand, the EDL current density $j_{EDL}(L_P,t)$ is defined as [44].

$$j_{EDL}(L_P,t) = -\varepsilon_0\varepsilon_r\frac{\partial^2\psi}{\partial x\partial t}(L_P,t) \tag{17}$$

where $\varepsilon_0 = 8.854 \times 10^{-12}$ F m^{-1} is the vacuum permittivity. On the other hand, the faradaic current density $j_F(L_P,t)$ can be computed from the generalized Frumkin-Butler-Volmer model evaluated at the electrode/electrolyte interface and expressed as [7].

$$j_F(L_P,t) = j_{F,0}(t)\left\{\exp\left[\frac{(1-\alpha)zF\eta(L_P,t)}{R_uT}\right] - \exp\left[\frac{-\alpha zF\eta(L_P,t)}{R_uT}\right]\right\} \tag{18}$$

where $j_{F,0}(t)$ is the so-called exchange current density and $R_u = 8.314$ J mol^{-1} K^{-1} is the universal gas constant. The exchange current density $j_{F,0}(t)$ can be written as [45,46].

$$j_{F,0}(t) = zFk_0[c_1(L_P,t)]^{1-\alpha}\left[c_{1,P,max} - c_{1,P}(L_P,t)\right]^{\alpha}\left[c_{1,P}(L_P,t)\right]^{\alpha}. \tag{19}$$

In addition, the surface overpotential $\eta(L_P,t)$ necessary to drive the redox reactions at the electrode/electrolyte interface can be expressed as [7].

$$\eta(L_P,t) = \Delta\psi_H(t) - \Delta\psi_{eq}(t) \tag{20}$$

where $\Delta\psi_H$ is the potential drop across the Stern layer of thickness $H = a/2$ and located between $x = L_P$ and $x = L_P + H$, i.e., $\Delta\psi_H(t) = \psi(L_P,t) - \psi(L_P + H,t)$ (Fig. 1).

The theoretical values of electrode R_P and electrolyte R_∞ resistances can be expressed as functions of the electrode thickness L_P and conductivity σ_P and of the electrolyte thickness L and conductivity σ_∞ according to [1,8].

$$R_P = L_P/\sigma_P \quad \text{and} \quad R_\infty \approx L/\sigma_\infty \quad \text{with} \quad \sigma_\infty = \left(2z^2F^2Dc_\infty\right)\Big/(R_uT). \tag{21}$$

The integral capacitance (in μF cm^{-2}) of pseudocapacitive electrodes associated with EDL formations $C_{int,EDL}$ or faradaic $C_{int,F}$ reactions can be evaluated by integrating the area enclosed by the CV curves respectively plotting the simulated currents $j_{EDL}(\psi_s)$ and $j_F(\psi_s)$versus the potential imposed $\psi_s(t)$ for a given scan rate ν [Equation (15)] according to [47],

$$C_{int,i}(\nu) = \oint \frac{j_i(\psi_s)}{2\nu(\psi_{s,max} - \psi_{s,min})}d\psi_s \quad \text{with} \quad i = T,\ EDL \text{ or } F. \tag{22}$$

The total integral capacitance $C_{int,T}$ of the electrode can be written as $C_{int,T}(\nu) = C_{int,EDL}(\nu) + C_{int,F}(\nu)$. Finally, the differential capacitance $C_{diff,i}$ (in μF cm^{-2}) is expressed as [10],

$$C_{diff,i} = \frac{j_i(\psi_s)}{\nu} \quad \text{with} \quad i = T,\ EDL \text{ or } F. \tag{23}$$

3.5. SPECS

3.5.1. SPECS fitting model

Combining Equations (3), (4) and (8), in absence of residual current (i.e., $j_r = 0$ A m^{-2}), yields the total current response $j_T^S(t)$ in a planar (i.e., non-porous) electrode for each potential step of the SPECS method [17,28],

$$j_T^S(t) = j_{EDL}^S(t) + j_F^S(t) = \frac{\Delta\psi_s}{R_{EDL}}\exp\left(-\frac{t}{R_{EDL}C_{EDL}}\right) + P_1\exp(-P_2t). \tag{24}$$

Here, the last term on the right hand side corresponds to the 1st term of the summation in Equation (8) that was retained since the higher terms were negligible [23], i.e.,

$$P_1 = 2\frac{\Delta Q_F}{\tau_d}\frac{\Lambda^2}{\Lambda^2 + \Lambda + b_1^2} \quad \text{and} \quad P_2 = \frac{b_1^2}{\tau_d}. \tag{25}$$

The superscript “S” refers to the SPECS fitting model to differentiate from the theoretical expressions of $j_{EDL}(t)$, $j_F(t)$, and $j_T(t)$ used in the numerical simulations [Equations (17) and (18)] and from $j_{EDL}^M(t)$, $j_F^M(t)$, and $j_T^M(t)$ determined from the MUSCA method [Equation (11)]. Equation (24) involves two time constant including (i) the EDL time constant τ_{EDL} which is relatively short and accounts for fast EDL formation and (ii) the diffusion time constant τ_d which is relatively long corresponding to slow diffusion process [16,23].

3.5.2. Fitting procedure

The nonlinear least-square regression was used to fit $j_T^S(t)$ to the numerical predictions of $j_T(t)$ obtained from the continuum MPNP model [48]. The four fitting parameters $R_{EDL}(\psi_s)$, $C_{EDL}(\psi_s)$, and $P_2(\psi_s)$ were positive and real numbers and $P_1(\psi_s)$ was positive during charging and negative during discharging. They were found for each potential ψ_s by minimizing the sum δ of the squared residuals for a given potential step as,

$$\delta = \sum_{i=1}^{n_s} \left[j_T(t_i) - j_T^S(t_i) \right]^2 . \tag{26}$$

Note that providing reasonable initial estimates of the fitting parameters was essential to find the global minimum of the objective function δ. Here, the initial guesses of R_{EDL} and C_{EDL} were respectively estimated as the internal resistance R_s obtained from EIS [Equation (21)] and as the total integral capacitance $C_{int,T}$ obtained from CV [Equation (22)] simulations for the same electrode and electrolyte properties and thicknesses.

4. Results and discussion

4.1. Electrochemical impedance spectroscopy

Fig. 2 shows the numerically predicted Nyquist plots for the simulated pseudocapacitive electrode for bias potential ψ_{dc} = -0.03 and 0.03 V. The oscillating potential amplitude was set as $\psi_0 = 5$ mV and the frequency f varied between 0.1 and 8×10^8 Hz. Note that, for practical porous electrodes, f usually varies between 0.1 and 1×10^5 Hz. However, the present study considered only a 1D planar electrode where relatively higher frequencies were required to capture the physicochemical phenomena associated with high frequency oscillations. Note also that the two semi-circles observed in the Nyquist plot were slightly depressed corresponding to the non-ideal capacitive behavior of the pseudocapacitive electrode due to redox reactions [49]. Based on the physical interpretation established by Mei et al. [9], the electrode resistance R_P was found to be 2 Ω cm^2 corresponding to the high-frequency intersection of the Nyquist plot with the Z_{re}-axis [8,9]. In addition, the electrolyte resistance R_∞ was 0.46 Ω cm^2 corresponding to the diameter of the semi-circle at high frequencies [8,9]. Both R_P and R_∞ were independent of bias potential ψ_{dc}. Moreover, the theoretical values of R_P and R_∞ predicted by Equation (21) were 2 and 0.5 Ω cm^2, respectively. The results confirm that EIS can predict the theoretical values of R_P and R_∞ relatively accurately. Finally, the internal resistance R_s is the summation of the electrode and bulk electrolyte resistances such that $R_s = R_P + R_\infty = 2.5$ Ω cm^2. Here, 2.5 Ω cm^2 was used as an initial guess for R_{EDL} in the fitting of the SPECS data, as previously mentioned.

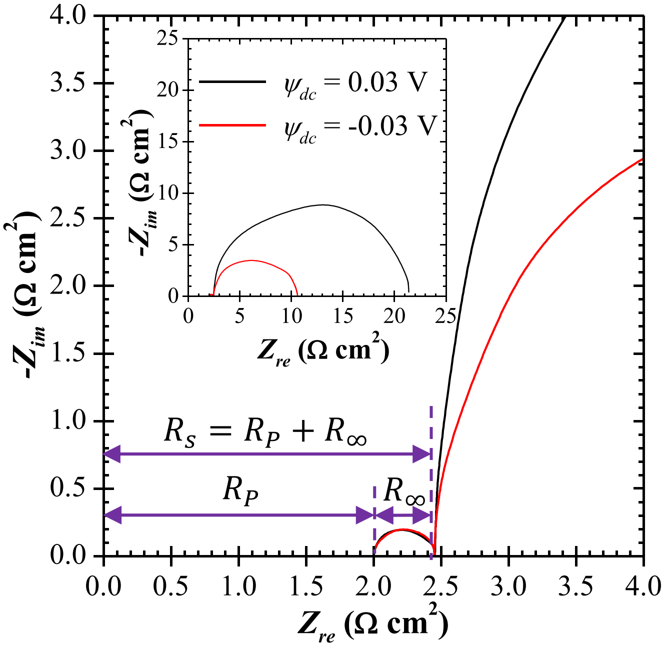

Fig. 2. Nyquist plot for the simulated pseudocapacitive electrode for bias potential ψ_{dc} = -0.03 and 0.03 V and frequency f varied between 0.1 and 8×10^8 Hz.

4.2. Cyclic voltammetry

Fig. 3(a) plots the numerically predicted CV curves for the pseudocapacitive electrode with potential window between $\psi_{s,min} = -0.05$ V and $\psi_{s,max} = 0.85$ V and scan rate ranging from ν = 0.1 to 5 V s^{-1}. First, Fig. 3(a) shows that the overall shapes of numerically simulated CV curves were similar to those experimentally measured for pseudocapacitive electrode consisting of nanocrystal film of orthorhombic niobium pentoxide (T-Nb_2O_5) in 1 M $LiClO_4$ in PC, as previously discussed in Ref. [50]. Note that, unlike actual porous electrodes, the simulated 1D planar electrode required relatively larger scan rates to exhibit Li^+ ion starvation and diffusion limitation [20]. Fig. 3(a) also indicates that the CV curves featured redox peaks during both charging and discharging. In addition, no significant drift with increasing scan rate was observed in these peaks suggesting that the redox reactions were highly reversible.

Fig. 3(b) shows the numerically simulated current densities j_T, j_{EDL}, and j_F versus potential ψ_s at oscillatory steady state for the pseudocapacitive electrode with potential window between -0.05 V and 0.85 V at scan rate $\nu = 2.5$ V s^{-1}. Fig. 3(b) indicates that the pseudocapacitive electrode featured two distinct regimes namely (i) a faradaic regime between -0.05 V and 0.25 V when $j_F(\psi_s) > j_{EDL}(\psi_s)$ and (ii) a capacitive (or EDL) regime between 0.25 V and 0.85 V when $j_{EDL}(\psi_s) > j_F(\psi_s)$. Note that the transition from faradaic to capacitive regime occurred at a potential ranging from 0.22 to 0.36 V as the scan rate decreases from 5 to 0.1 V s^{-1} (see Supplementary Materials).

The so-called b-value characterizes the power law evolution of the total current $j_T(\psi_s)$ with respect to scan rate ν for a given potential ψ_s in cyclic voltammetry. Fig. 3(c) shows the b-value as a function of potential ψ_s calculated by the least-squares method fitting $j_T(\psi_s)$ vs. ν obtained from Fig. 3(a) to the expression [35],

$$j_T(\psi_s) = a(\psi_s)\, \nu^{b(\psi_s)} \tag{27}$$

where $a(\psi_s)$ and $b(\psi_s)$ are fitting parameters. The dip in the b-value around $\psi_s = 0.25$ V corresponds to the transition between the capacitive and faradaic regimes, as established by Girard et al. [35].

Fig. 3(d) plots the EDL $C_{int,EDL}$, faradaic $C_{int,F}$, and total $C_{int,T}$ integral capacitances [Equation (22)] for the pseudocapacitive electrode as functions of scan rate ν ranging from 0.1 to 5 V s^{-1}. Here, $C_{int,EDL}(\nu)$ was independent of scan rate corresponding to quasi-equilibrium conditions, as previously observed in simulations of planar [32] and porous [51] electrodes. On the other hand, the faradaic capacitance $C_{int,F}(\nu)$ decreased with increasing scan rate due to relatively slow Li^+ intercalation in the electrode compared with fast EDL formation. Similar behavior was observed experimentally for other pseudocapacitive electrodes [50,52–54]. Finally, the average of $C_{int,T}$ over the different scan rates was used as initial guess for C_{EDL} in the SPECS method, as previously discussed.

4.3. SPECS validation

Fig. 4(a) shows the imposed potential as a function of time used in numerical simulations of the SPECS method and consisting of a series of small potential steps of $\Delta\psi_s = 0.02$ V with equilibration

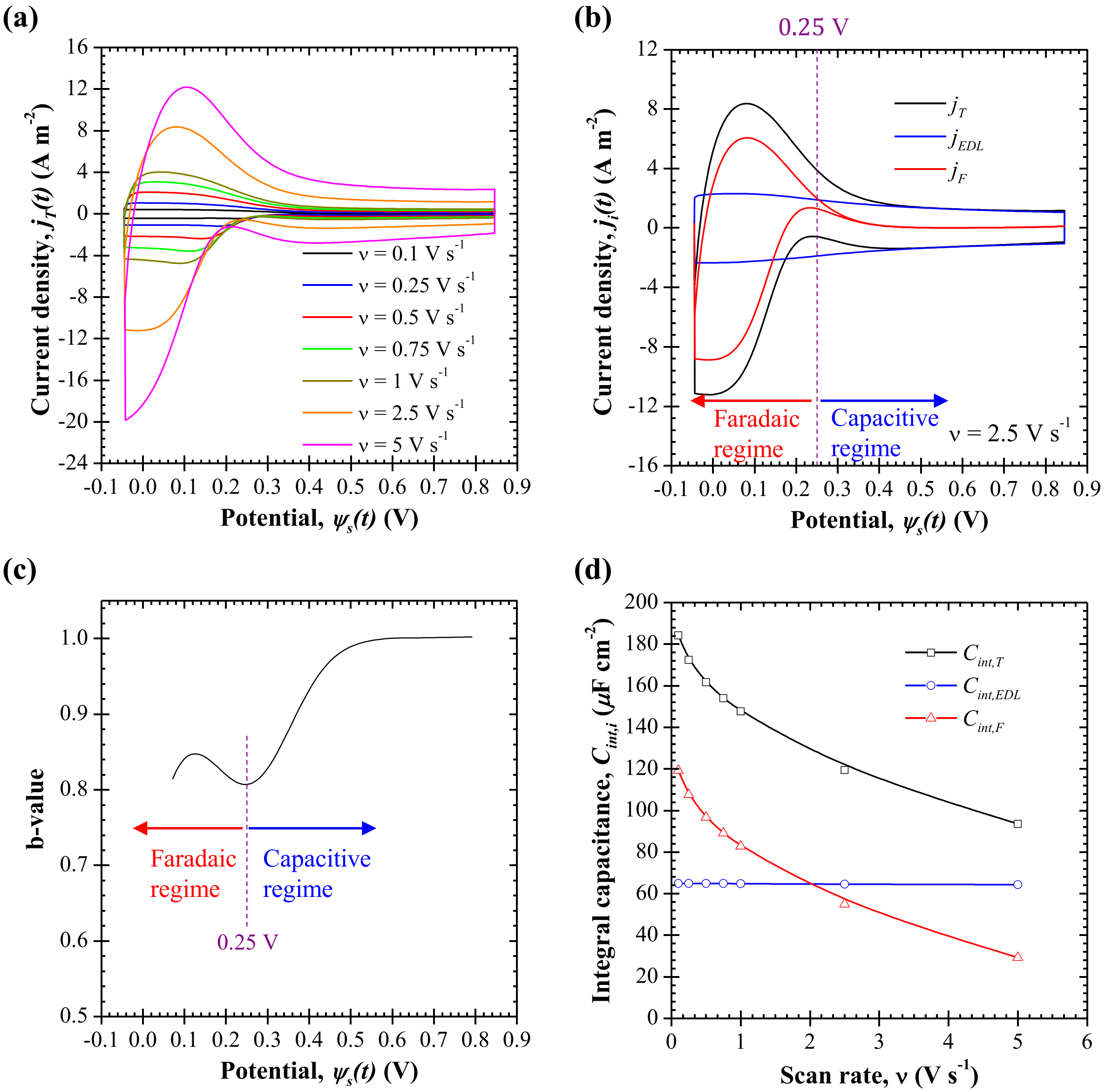

Fig. 3. (a) Numerically predicted CV curves for the simulated pseudocapacitive electrode with potential window between $\psi_{s,min} = -0.05$ V and $\psi_{s,max} = 0.85$ V for scan rate ranging from $\nu = 0.1$ to 5 V s^{-1}. (b) Total j_T, EDL j_{EDL}, and faradaic j_F current densities versus potential ψ_s at scan rate $\nu = 2.5$ V s^{-1}. (c) *b*-value as a function of potential ψ_s. (d) Integral capacitance $C_{int,i}$ for the pseudocapacitive electrode as a function of scan rate ν ranging from 0.1 to 5 V s^{-1}.

time $t_e = 0.2$ s. Here also, the equilibration time t_e of the SPECS simulations was much smaller than that of the actual measurements for porous pseudocapacitive electrodes [16,17,24]. This was due to the fact that the charging/discharging processes reached equilibrium much faster in the simulated planar electrode than in actual porous pseudocapacitive electrodes. To avoid discontinuity in the potential $\psi(x,t)$ and the associated numerical instabilities at the transition from one step to another, the potential step was smoothed using a polynomial function with a continuous second order derivative during a transition time $t_t = 50\ \mu$s, as illustrated in the inset of Fig. 4(a).

Fig. 4(b) plots the computed current density response $j_T(t)$ to the potential steps of Fig. 4(a) as a function of time. It also plots the numerically predicted current densities due to EDL formation $j_{EDL}(t)$ [Equation (17)] and faradaic reactions $j_F(t)$ [Equation (18)] such that $j_T(t) = j_{EDL}(t) + j_F(t)$. Here, the current densities were recorded at each time step $\Delta t = 10\ \mu$s to provide sufficient data points for the fitting procedure [29]. It is interesting to note that the behavior of $j_T(t)$ simulated was remarkably similar to that measured experimentally [16,17,24].

Fig. 5 plots the temporal evolution of the numerically predicted total current density $j_T(t)$ [Equations (17) and (18)] and of the mathematically fitted SPECS model j_T^S [Equation (24)] for potential step $\Delta\psi_s = 0.02$ V at (a) $\psi_s = 0.09$ V and (b) $\psi_s = 0.51$ V. These values of cell potential were chosen to fall in the faradaic and capacitive regimes, respectively. It is reassuring to note that $j_T^S(t)$ obtained after fitting the SPECS simulations was in good agreement with the simulated current $j_T(t)$ for both potential values. The insets display the data in log scale to highlight the good agreement between $j_T(t)$ and $j_T^S(t)$ over a large temporal window. The results show that 95% of the SPECS model data fell within ±0.2 A m^{-2} of the simulated current density confirming the quality of the fit. However, good fitting between $j_T(t)$ and $j_T^S(t)$ does not guarantee

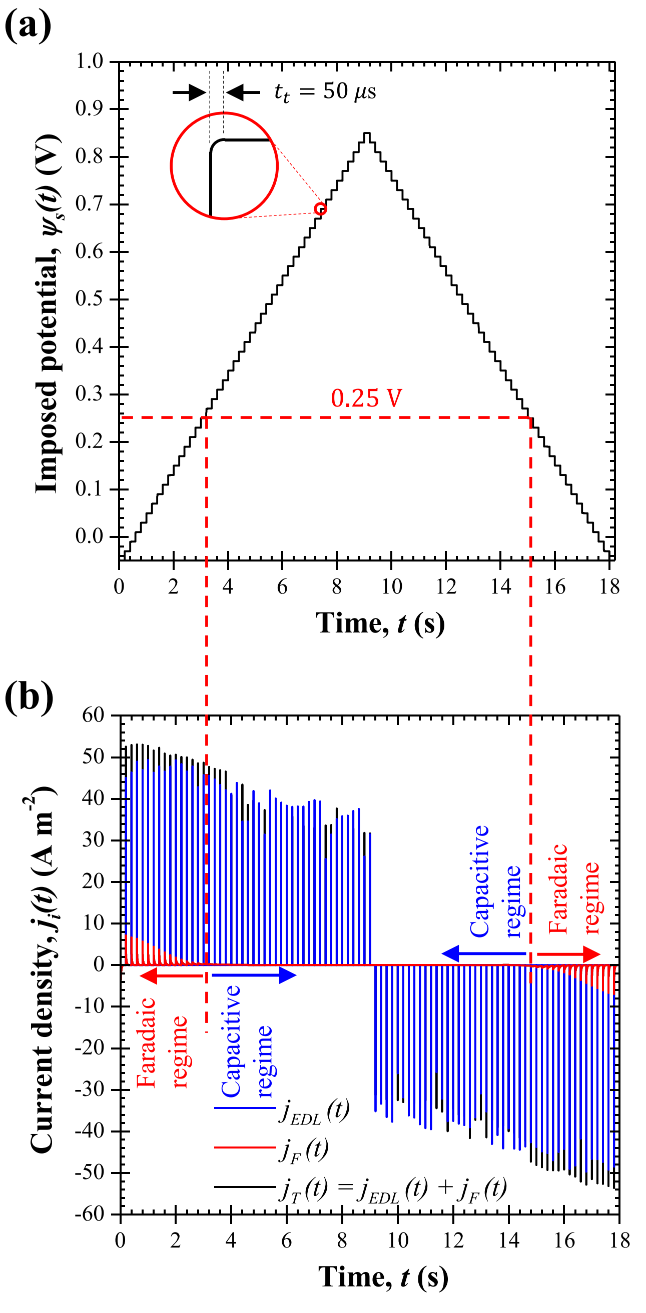

Fig. 4. (a) Imposed step potential as a function of time for step size $\Delta\psi_s =$ 0.02 V and relaxation time $t_r = 0.2$ s. (b) Total $j_T(t)$, EDL $j_{EDL}(t)$, and faradaic $j_F(t)$ current densities in response to the step potentials as functions of time.

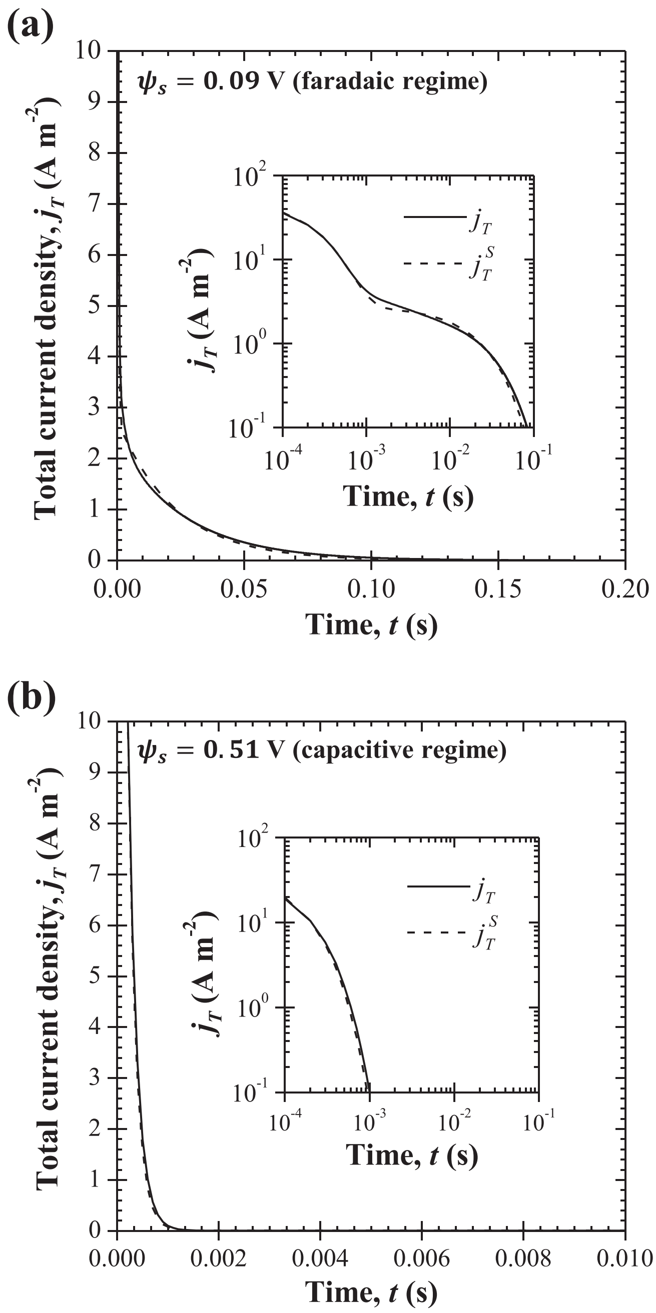

Fig. 5. Numerically predicted total current density $j_T(t)$ [Equations (17) and (18)] and mathematically fitted SPECS model $j_T^S(t)$ [Equation (24)] for potential step $\Delta\psi_s = 0.02$ V at (a) $\psi_s = 0.09$ V (faradaic regime) and (b) $\psi_s = 0.51$ V (capacitive or EDL regime).

that $j_{EDL}(t)$ and $j_F(t)$ were predicted accurately.

Fig. 6 shows the simulated EDL $j_{EDL}(t)$ and faradaic $j_F(t)$ current densities as functions of time at (a) $\psi_s = 0.09$ V and (b) $\psi_s = 0.51$ V for $\Delta\psi_s = 0.02$ V. It also plots the predictions of j_{EDL}^S [Equation (4)] and j_F^S [Equation (8)] based on the parameters obtained by fitting $j_T^S(t)$ to $j_T(t)$. It is interesting to note that both current densities j_{EDL}^S and j_F^S retrieved from the SPECS method were in good agreement with the numerically computed current densities $j_{EDL}(t)$ and $j_F(t)$ using Equations (17) and (18), respectively. In fact, the associated maximum root-mean-square-error was ±0.2 A m^{-2} and ±0.1 A m^{-2}, respectively. At the beginning of each step, the current densities featured spikes due to fast ion transport in response to the sudden potential step $\Delta\psi_s = 0.02$ V. The spike in $j_{EDL}(t)$ was always higher than that in $j_F(t)$. However, $j_{EDL}(t)$ decayed faster than $j_F(t)$ corresponding to a shorter EDL time constant τ_{EDL} compared with diffusion time constant τ_d since EDL formation/dissolution was much faster than the redox reactions and Li$^+$ intercalation.

Finally, note that the Cottrell relation [Equation (5)] was also used to fit the total current density $j_T(t)$. Unfortunately, the results show a substantial disagreement between $j_F(t)$ and j_F^S confirming that the Cottrell relation was not valid for long time (i.e., $t \gg \tau_d$) [23] (see Supplementary Materials).

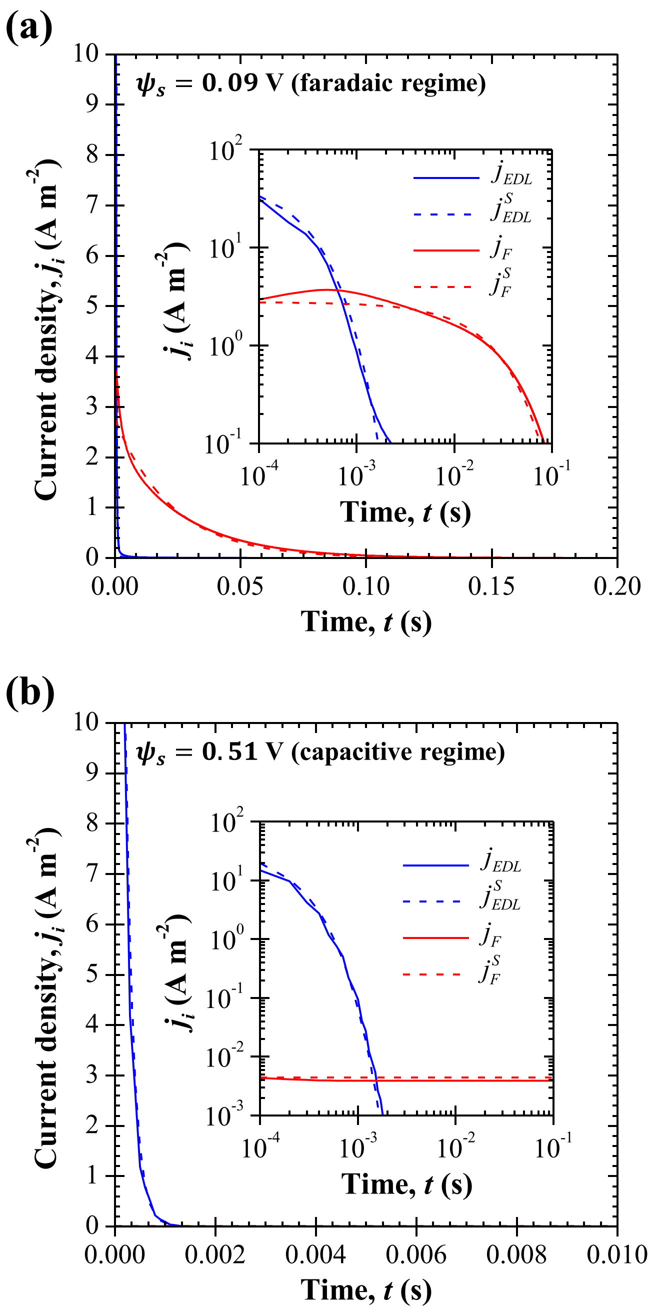

Fig. 6. Numerically predicted EDL j_{EDL} and faradaic j_F current densities along with their corresponding j^S_{EDL} and j^S_F estimated by Equations (4) and (8), respectively, using the SPECS fitting parameters plotted in Fig. 7 at (a) $\psi_s = 0.09$ V and (b) $\psi_s = 0.51$ V.

4.4. SPECS parameters interpretation

Fig. 7 plots the fitting parameters (a) R_{EDL}, (b) C_{EDL}, (c) $|P_1|$, and (d) P_2 as functions of imposed potential ψ_s for potential steps $\Delta\psi_s =$ 0.01, 0.02, and 0.04 V. First, Fig. 7 establishes that the values of all fitting parameters during charging were identical to that during discharging for a given potential step. In addition, R_{EDL}, C_{EDL}, $|P_1|$, and P_2 were nearly continuous functions of ψ_s and consistent from one potential step to the next. They were also independent of potential step $\Delta\psi_s$ except for $|P_1|$ which increased with increasing $\Delta\psi_s$. However, the ratio $P_1^* = |P_1|/\Delta\psi_s$ was independent of $\Delta\psi_s$ (see inset of Fig. 7(c)). This observation can be attributed to the fact that ΔQ_F was proportional to $\Delta\psi_s$.

Fig. 7(a) indicates that the resistance R_{EDL} was nearly independent of the imposed potential ψ_s. In addition, its average value of $\overline{R}_{EDL} = 2.86 \pm 0.4\ \Omega\ \text{cm}^2$ was in satisfactory agreement with the internal resistance of the electrode ($R_s = 2.5\ \Omega\ \text{cm}^2$) theoretically predicted by Equation (21) and with the value retrieved from EIS simulations ($R_P + R_\infty = 2.45\ \Omega\ \text{cm}^2$). Here, the error associated with $\overline{R}_{EDL}$ corresponds to two standard deviations or 95% confidence interval estimated by averaging R_{EDL} for $\Delta\psi_s = 0.02$ V.

Fig. 7(b) shows that C_{EDL} decreased from 100 to 40 μF cm^{-2} with imposed potential ψ_s increasing from −0.05 to 0.85 V. The fitted capacitance C_{EDL} was in excellent agreement with the differential capacitance $C_{diff,EDL}$ [Equation (23)] computed from CV simulations [Fig. 3(b)]. In fact, during charging, the anion concentration $c_2(t)$ increased due to EDL formation approaching its maximum value $c_{2,max} = 1/N_A a_2^3 = 5.52$ mol L^{-1} [55]. Then, the ion accumulation rate at the electrode/electrolyte interface decreased with increasing imposed potential ψ_s. As a result, the EDL current density j_{EDL} also decreased with increasing imposed potential ψ_s corresponding to the narrowing region observed in the CV curve of j_{EDL} at high potential [Fig. 3(b)]. Note that $C_{diff,EDL}$ was independent of scan rate ν (quasi-equilibrium regime). Finally, the averaged value of C_{EDL} over the entire potential window $\overline{C}_{EDL} = 68\ \mu$F cm^{-2} retrieved using the SPECS method was in good agreement with the integral capacitance $C_{int,EDL} = 65\ \mu$F cm^{-2} predicted by CV simulation and independent of ν (Fig. 3(d)).

Finally, Figs. 7(c) and 7(d) indicate that $|P_1|$ and P_2 were strongly dependent on the charging/discharging regime. In fact, they decayed quickly with increasing potential and reached zero around the transition potential $\psi_s \simeq 0.25$ V separating the faradaic from the capacitive regime. Indeed, $|P_1|$ is a function of stored charges due to the faradaic reaction contributions ΔQ_F which vanishes in the capacitive regime for $\psi_s \gtrsim 0.25$ V. In addition, P_2 is a function of the parameters b_n and of the diffusion time constant τ_d. Equation (6) establishes that τ_d is independent of potential. On the other hand, b_n is a function of Λ [Equation (9)] which strongly depends on the charge storage mechanism, as discussed earlier. Thus, the value of P_2 decreased as the charge storage mechanism varied from diffusion controlled (i.e., $\Lambda \gg 1$) in the faradaic regime to interfacial charge transfer kinetics controlled (i.e., $\Lambda \ll 1$) in the capacitive regime. These results provide further evidence of the existence of the capacitive and faradaic regimes first elucidated by Girard et al. [35]. It is also consistent with the physical interpretation of the dip observed in the b-value [Fig. 3(c)] [21,35].

4.5. MUSCA method

Fig. 8(a) plots $j_{EDL}(\psi_s)$ and $j_F(\psi_s)$ computed numerically as well as $j_C(\psi_s)$ and $j_D(\psi_s)$ obtained using the k_1, k_2 analysis on CV simulations versus potential ψ_s for scan rate $\nu = 2.5$ V s^{-1} shown in Fig. 3(b). It indicates that the shape of $j_C(\psi_s)$ and $j_D(\psi_s)$ estimated by performing the k_1, k_2 analysis on the numerically predicted CV curves were inconsistent with $j_{EDL}(\psi_s)$ and $j_F(\psi_s)$ predicted by the MPNP model. In other words, the k_1, k_2 analysis cannot distinguish between contributions from EDL formation and faradaic reactions directly from CV curves which suffer from ohmic polarization.

Fig. 8(b) plots the calculated CV curves $j_T^M(\psi_s)$ obtained from previous SPECS simulations [Fig. 4(b)] and processed using the MUSCA method [Equation (11)] for scan rate ν [Equation (12)] ranging from 0.1 to 5 V s^{-1}. Here, it is interesting to note that the redox peaks were almost aligned regardless of the scan rate considered. In addition, the CV curves were more symmetric around $j_T^M = 0$, compared with Fig. 3(a). This confirmed that the

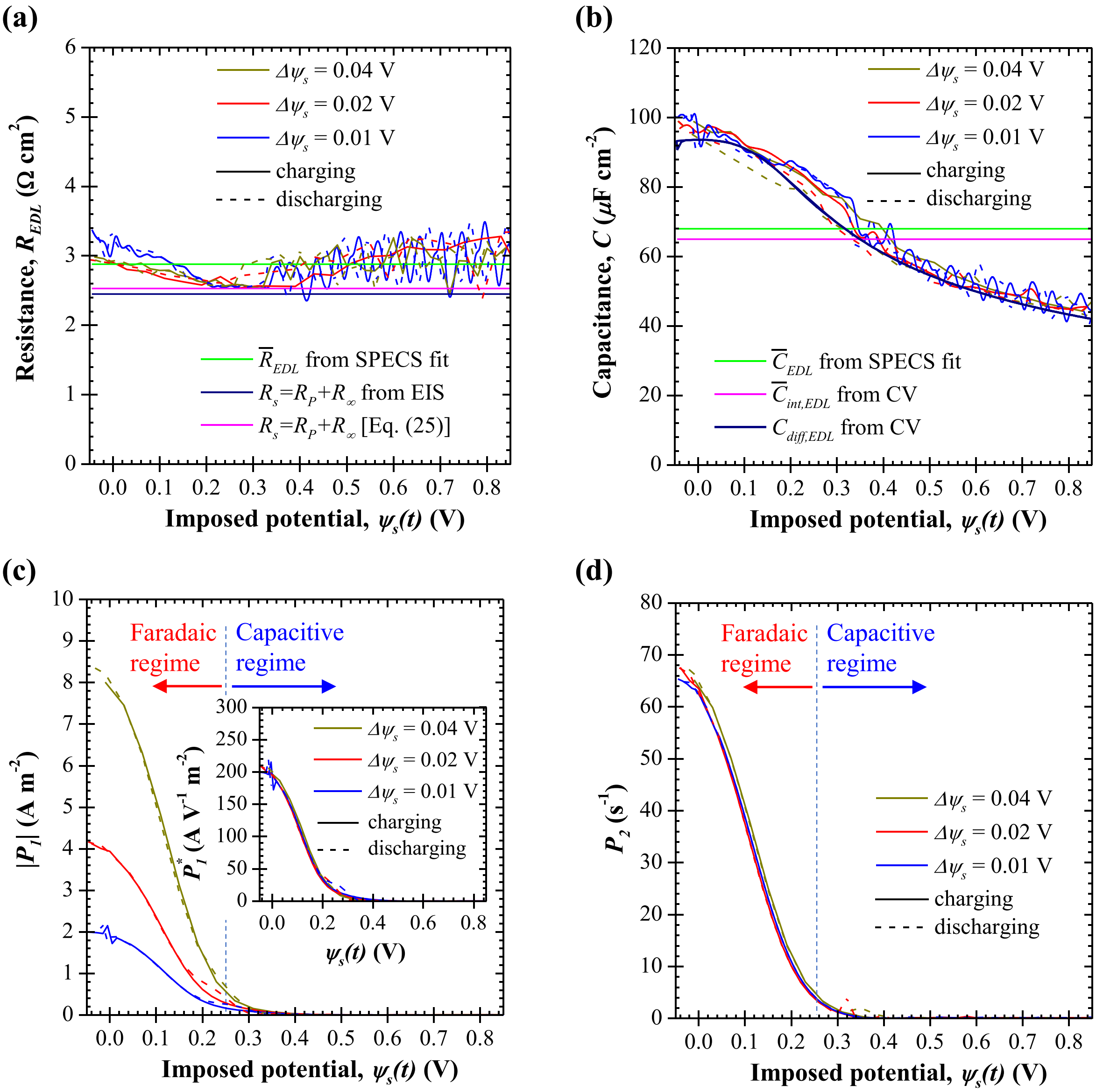

Fig. 7. Fitting parameters of the SPECS method (a) R_{EDL}, (b) C_{EDL}, (c) $|P_1|$ and in inset $P_1^* = |P_1|/\Delta\psi_s$, and (d) P_2 as functions of imposed potential ψ_s for potential steps $\Delta\psi_s =$ 0.01, 0.02, and 0.04 V.

effect of ohmic polarization and residual current were minimized by allowing the current density to fully decay to the equilibrium conditions. These results have also been observed experimentally for Ti$_3$C$_2$T$_x$ MXene electrode in 3 M H$_2$SO$_4$ electrolyte [19].

Moreover, the k_1, k_2 analysis was used to estimate the capacitive j_C^M and diffusion j_D^M current density contributions to the total current density j_T^M corrected using the MUSCA method. Fig. 8(c) plots $j_{EDL}^M(\psi_s)$, $j_F^M(\psi_s)$, j_C^M, and j_D^M obtained using the MUSCA method versus potential ψ_s for scan rate $\nu = 2.5$ V s^{-1}. It shows that j_C^M and j_D^M were similar to $j_{EDL}^M(t)$ and $j_F^M(t)$ reconstructed from the MUSCA method. The same results were observed for other scan rates (see Supplementary Materials).

Finally, the integral capacitance can be defined by Equation (22) for all currents predicted numerically (e.g., j_{EDL}, j_F) or retrieved from the MUSCA method [Equation (11)] (e.g., j_{EDL}^M, j_F^M) or from the k_1, k_2 analysis (e.g., j_C, j_D, j_C^M, j_D^M) [Equation (2)]. Fig. 8(d) plots, as functions of scan rate ν, the ratios of (i) the integral capacitive capacitance to EDL capacitance $C_{int,C}/C_{int,EDL}$ and diffusive capacitance to faradaic capacitance $C_{int,D}/C_{int,F}$ evaluated using the CV curves obtained numerically [Fig. 3(a)] and of (ii) the capacitive capacitance to EDL capacitance $C_{int,C}^M/C_{int,EDL}^M$ and diffusive capacitance to faradaic capacitance $C_{int,D}^M/C_{int,F}^M$ evaluated using the CV curves generated by the MUSCA method [Fig. 8(b)]. It indicates that $C_{int,EDL}$ and $C_{int,F}$ were significantly different from capacitive $C_{int,C}$ and diffusive $C_{int,D}$ capacitances estimated from the k_1, k_2 analysis directly from the CV curves. However, for all scan rates considered, the capacitances $C_{int,C}^M$ and $C_{int,D}^M$ were in good agreement with $C_{int,EDL}^M$ and $C_{int,F}^M$, respectively, based on CV curves generated by the MUSCA method. Therefore, the k_1, k_2 analysis provided good estimates of the EDL contribution (i.e., $j_C \simeq j_{EDL}$) and faradaic reactions contribution (i.e., $j_D \simeq j_F$) when it was applied to the CV curves reconstructed using the MUSCA method.

Note that the present study considered planar electrodes while

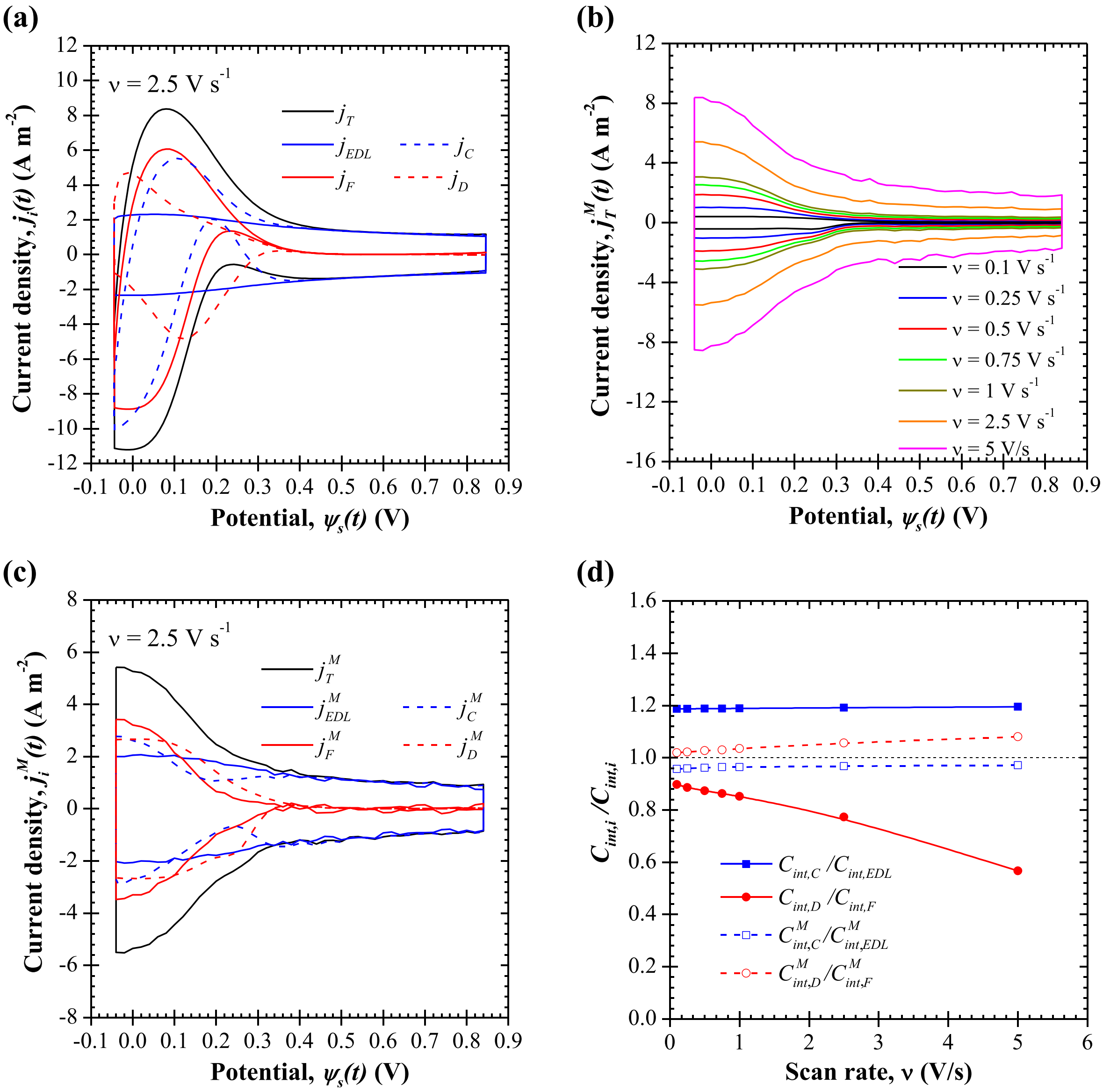

Fig. 8. (a) $j_{EDL}(\psi_s)$, $j_F(\psi_s)$, $j_C(\psi_s)$, and $j_D(\psi_s)$ obtained using the k_1, k_2 analysis on CV simulations versus potential ψ_s for scan rate $\nu = 2.5$ V s^{-1}. (b) Reconstructed CV curves from SPECS simulations (Fig. 4(b)) using the MUSCA method for scan rate ranging from $\nu = 0.1$ to 5 V s^{-1}. (c) $j^M_{EDL}(\psi_s)$, $j^M_F(\psi_s)$, j^M_C, and j^M_D obtained using the MUSCA method versus potential ψ_s for scan rate $\nu = 2.5$ V s^{-1}. (d) Ratios of integral capacitances $C_{int,i}/C_{int,i}$ as functions of scan rate ν.

practical pseudocapacitive electrodes are porous. First, our simulations for planar electrodes qualitatively reproduce experimental cyclic voltammogram for pseudocapacitive electrodes. This indicates that the model accounts for the key physical phenomena. The physical model discussed in the present study can be extended to porous electrodes in three-dimensional simulations but at significant computational cost [51]. Alternatively, the present study could be used to develop volume-averaged continuum models for porous electrode with some effective transport properties. Also, note that the present physical model accounts for faradaic current involving (i) surface redox reactions governed by the generalized Frumkin-Butler-Volmer model [Equation (S.11)] and (ii) ion intercalation/deintercalation governed by Fick's law of diffusion [Equation (S.4)]. The two mechanisms were captured in the numerically simulated j_F which was successfully determined by the SPECS and MUSCA methods. Thus, the SPECS and MUSCA methods apply to pseudocapacitive electrodes involving fast surface redox and/or ion intercalation/deintercalation.

5. Conclusion

In this paper, the SPECS and MUSCA methods were theoretically and rigorously validated using a continuous model based on the modified Poisson-Nernst-Planck model coupled with Frumkin-Butler-Volmer theory. The model was solved numerically to predict the current density response to a series of potential steps across a realistic potential window so as to reproduce the SPECS method for a 1D planar pseudocapacitive electrode in three-electrode configuration. First, the numerically predicted total current density j_T was qualitatively similar to the typical experimental measurements obtained from the SPECS method. Moreover, the capacitive and faradaic current densities estimated from the SPECS fitting procedure were found to be in excellent agreement with those defined in the continuum model and computed numerically.

In addition, the internal resistance R_s and the differential EDL capacitance $C_{diff,EDL}$ obtained from CV and EIS simulations, respectively, were also in good agreement with those obtained by the SPECS method to model the EDL current based on resistor and capacitor in series. Moreover, the SPECS method was capable of identifying the faradaic and capacitive (or EDL) regimes during charging via the fitting parameters used to model the faradaic current. The results were consistent with the analysis of the b-value obtained from CV curves at different scan rates. Finally, the MUSCA method was found to successfully minimize the effect of ohmic polarization on CV curves by correcting for the redox peak drift observed experimentally. In addition, the capacitive and diffusive current densities retrieved from the k_1, k_2 analysis on CV curves produced by the MUSCA method was in good agreement with EDL and faradaic current densities reconstructed from the MUSCA method.

Acknowledgment

This work was supported as part of the Center for Synthetic Control Across Length-scales for Advancing Rechargeables (SCALAR), an Energy Frontier Research Center funded by the U.S. Department of Energy, Office of Science, Basic Energy Sciences under Award # DE-SC0019381. O.M. is grateful for the the graduate fellowship provided by King Fahd University of Petroleum and Minerals (KFUPM), Dhahran, Saudi Arabia.

Appendix A. Supplementary data

Supplementary data to this article can be found online at https://doi.org/10.1016/j.electacta.2019.134648.

References

[1] B. Conway, Electrochemical Supercapacitors: Scientific Fundamentals and Technological Applications, Kluwer Academic/Plenum, New York, NY, 1999.
[2] B.E. Conway, V. Birss, J. Wojtowicz, The role and utilization of pseudocapacitance for energy storage by supercapacitors, J. Power Sources 66 (1–2) (1997) 1–14.
[3] M.R. Lukatskaya, B. Dunn, Y. Gogotsi, Multidimensional materials and device architectures for future hybrid energy storage, Nat. Commun. 7 (2016) 1–13.
[4] V. Augustyn, P. Simon, B. Dunn, Pseudocapacitive oxide materials for high-rate electrochemical energy storage, Energy Environ. Sci. 7 (5) (2014) 1597–1614.
[5] J.B. Cook, H.S. Kim, T.C. Lin, C.H. Lai, B. Dunn, S.H. Tolbert, Pseudocapacitive charge storage in thick composite MoS_2 nanocrystal-based electrodes, Adv. Energy Mater. 7 (2) (2017) 1601283.
[6] M. Toupin, T. Brousse, D. Belanger, Charge storage mechanism of MnO_2 electrode used in aqueous electrochemical capacitor, Chem. Mater. 16 (16) (2004) 3184–3190.
[7] A.J. Bard, L.R. Faulkner, Electrochemical Methods: Fundamentals and Applications, second ed., Wiley & Sons, New York, NY, 1980.
[8] B.-A. Mei, O. Munteshari, J. Lau, B. Dunn, L. Pilon, Physical interpretations of Nyquist plots for EDLC electrodes and devices, J. Phys. Chem. C 122 (1) (2018) 194–206.
[9] B.-A. Mei, J. Lau, T. Lin, S.H. Tolbert, B. Dunn, L. Pilon, Physical interpretations of electrochemical impedance spectroscopy of redox active electrodes for electrical energy storage, J. Phys. Chem. C 122 (2018) 24499–24511.
[10] H. Wang, L. Pilon, Reply to comments on “Intrinsic limitations of impedance measurements in determining electric double layer capacitances” by H. Wang, L. Pilon [Electrochimica Acta 63 (2012) 55], Electrochim. Acta 76 (2012) 529–531.
[11] C. Lei, F. Markoulidis, Z. Ashitaka, C. Lekakou, Reduction of porous carbon/Al contact resistance for an electric double-layer capacitor (EDLC), Electrochim. Acta 92 (2013) 183–187.
[12] M. Arulepp, L. Permann, J. Leis, A. Perkson, K. Rumma, A. Jänes, E. Lust, Influence of the solvent properties on the characteristics of a double layer capacitor, J. Power Sources 133 (2) (2004) 320–328.
[13] E. Barsoukov, J.R. Macdonald, Impedance Spectroscopy: Theory, Experiment, and Applications, John Wiley & Sons, New York, NY, 2018.
[14] T.-C. Liu, W.G. Pell, B.E. Conway, S.L. Roberson, Behavior of molybdenum nitrides as materials for electrochemical capacitors, J. Electrochem. Soc. 145 (6) (1998) 1882–1888.
[15] T. Brezesinski, J. Wang, S.H. Tolbert, B. Dunn, Ordered mesoporous α-MoO_3 with iso-oriented nanocrystalline walls for thin-film pseudocapacitors, Nat. Mater. 9 (2) (2010) 146–151.
[16] M.F. Dupont, S.W. Donne, Faradaic and non-faradaic contributions to the power and energy characteristics of electrolytic manganese dioxide for electrochemical capacitors, J. Electrochem. Soc. 163 (6) (2016) A888–A897.
[17] M.F. Dupont, S.W. Donne, Charge storage mechanisms in electrochemical capacitors: effects of electrode properties on performance, J. Power Sources 326 (2016) 613–623.
[18] M.F. Dupont, S.W. Donne, Electrolytic manganese dioxide structural and morphological effects on capacitive performance, Electrochim. Acta 191 (2016) 479–490.
[19] H. Shao, Z. Lin, K. Xu, P.L. Taberna, P. Simon, Electrochemical study of pseudocapacitive behavior of $Ti_3C_2T_x$ MXene material in aqueous electrolytes, Energy Storage Mater. 18 (2019) 456–461.
[20] H.L. Girard, B. Dunn, L. Pilon, Simulations and interpretation of three-electrode cyclic voltammograms of pseudocapacitive electrodes, Electrochim. Acta 211 (2016) 420–429.
[21] B.-A. Mei, B. Li, J. Lin, L. Pilon, Multidimensional cyclic voltammetry simulations of pseudocapacitive electrodes with a conducting nanorod scaffold, J. Electrochem. Soc. 164 (13) (2017) A3237–A3252.
[22] J.C. Wen, B.A. Boukamp, R.A. Huggins, W. Weppner, Thermodynamic and mass transport properties of LiAl, J. Electrochem. Soc. 126 (12) (1979) 2258.
[23] C. Montella, Discussion of the potential step method for the determination of the diffusion coefficients of guest species in host materials: Part I. Influence of charge transfer kinetics and ohmic potential drop, J. Electroanal. Chem. 518 (2) (2002) 61–83.
[24] M.F. Dupont, S.W. Donne, A step potential electrochemical spectroscopy analysis of electrochemical capacitor electrode performance, Electrochim. Acta 167 (2015) 268–277.
[25] M.F. Dupont, S.W. Donne, Separating the faradaic and non-faradaic contributions to the total capacitance for different manganese dioxide phases, J. Electrochem. Soc. 162 (5) (2015) A5096–A5105.
[26] M.A. Hughes, J.A. Allen, S.W. Donne, The properties and performance of carbon produced through the electrochemical reduction of molten carbonate: a study based on step potential electrochemical spectroscopy, Electrochim. Acta 278 (2018) 340–351.
[27] M. Forghani, S.W. Donne, Method comparison for deconvoluting capacitive and pseudo-capacitive contributions to electrochemical capacitor electrode behavior, J. Electrochem. Soc. 165 (3) (2018) A664–A673.
[28] M.F. Dupont, M. Forghani, A.P. Cameron, S.W. Donne, Effect of electrolyte cation on the charge storage mechanism of manganese dioxide for electrochemical capacitors, Electrochim. Acta 271 (2018) 337–350.
[29] Y. Jiang, C. Hall, N. Song, D. Lau, P.A. Burr, R. Patterson, D.-W. Wang, Z. Ouyang, A. Lennon, Evidence for fast lithium-ion diffusion and charge-transfer reactions in amorphous TiO_x nanotubes: insights for high-rate electrochemical energy storage, ACS Appl. Mater. Interfaces 10 (2018) 42513–42523.
[30] M.Z. Bazant, M.S. Kilic, B.D. Storey, A. Ajdari, Towards an understanding of induced-charge electrokinetics at large applied voltages in concentrated solutions, Adv. Colloid Interface Sci. 152 (1–2) (2009) 48–88.
[31] R. Qiao, N.R. Aluru, Ion concentrations and velocity profiles in nanochannel electroosmotic flows, J. Chem. Phys. 118 (10) (2003) 4692–4701.
[32] H. Wang, A. Thiele, L. Pilon, Simulations of cyclic voltammetry for electric double layers in asymmetric electrolytes: a generalized modified Poisson-Nernst-Planck model, J. Phys. Chem. C 117 (36) (2013) 18286–18297.
[33] J.H. Masliyah, S. Bhattacharjee, Electrokinetic and Colloid Transport Phenomena, John Wiley & Sons, Hoboken, NJ, 2006.
[34] M.Z. Bazant, K. Thornton, A. Ajdari, Diffuse-charge dynamics in electrochemical systems, Phys. Rev. E 70 (2) (2004) 21506.
[35] H.-L. Girard, H. Wang, A.L. d'Entremont, L. Pilon, Physical interpretation of cyclic voltammetry for hybrid pseudocapacitors, J. Phys. Chem. C 119 (21) (2015) 11349–11361.
[36] K. Nishikawa, Y. Fukunaka, T. Sakka, Y.H. Ogata, J.R. Selman, Measurement of $LiClO_4$ diffusion coefficient in propylene carbonate by Moiré Pattern, J. Electrochem. Soc. 153 (5) (2006) A830–A834.
[37] G.J. Janz, R.P.T. Tomkins, Nonaqueous Electrolytes Handbook, vol. I, Academic Press, New York, NY, 1972.
[38] A.M. Colclasure, R.J. Kee, Thermodynamically consistent modeling of elementary electrochemistry in lithium-ion batteries, Electrochim. Acta 55 (28) (2010) 8960–8973.
[39] P. Guillemet, T. Brousse, O. Crosnier, Y. Dandeville, L. Athouel, Y. Scudeller, Modeling pseudocapacitance of manganese dioxide, Electrochim. Acta 67 (2012) 41–49.
[40] Q. Zhong, B. Huang, J. Ma, H. Li, Experimental study on relationship between SOC and OCV of lithium-ion batteries, Int. J. Smart Grid Clean Energy 3 (2) (2014) 149–153.
[41] T.R. Jow, J.P. Zheng, Electrochemical capacitors using hydrous ruthenium oxide and hydrogen inserted ruthenium oxide, J. Electrochem. Soc. 145 (1) (1998) 49–52.
[42] G. Sikha, R.E. White, B.N. Popov, A mathematical model for a lithium-ion battery/electrochemical capacitor hybrid system, J. Electrochem. Soc. 152 (8) (2005) 1682–1693.
[43] H. Kim, B.N. Popov, A mathematical model of oxide, carbon composite electrode for supercapacitors, J. Electrochem. Soc. 150 (9) (2003) 1153–1160.
[44] H. Cohen, J.W. Cooley, The numerical solution of the time-dependent Nernst-Planck equations, Biophys. J. 5 (2) (1965) 145–162.
[45] V.R. Subramanian, V. Boovaragavan, V. Ramadesigan, M. Arabandi,

Mathematical model reformulation for lithium-ion battery simulations: galvanostatic boundary conditions, J. Electrochem. Soc. 156 (4) (2009) A260–A271.

[46] G.M. Goldin, A.M. Colclasure, A.H. Wiedemann, R.J. Kee, Three-dimensional particle-resolved models of Li-ion batteries to assist the evaluation of empirical parameters in one-dimensional models, Electrochim. Acta 64 (2012) 118–129.

[47] R.T. Wen, C.G. Granqvist, G.A. Niklasson, Eliminating degradation and uncovering ion-trapping dynamics in electrochromic WO_3 thin films, Nat. Mater. 14 (10) (2015) 996–1001.

[48] D.C. Sorensen, “Newton's method with a model trust region modification”, SIAM J. Numer. Anal. 19 (2) (1982) 409–426.

[49] A. Allagui, T.J. Freeborn, A.S. Elwakil, B.J. Maundy, Reevaluation of performance of electric double-layer capacitors from constant-current charge/discharge and cyclic voltammetry, Sci. Rep. 6 (2016) 38568.

[50] V. Augustyn, J. Come, M.A. Lowe, J.W. Kim, P. Taberna, S.H. Tolbert, H.D. Abruña, P. Simon, B. Dunn, High-rate electrochemical energy storage through Li_+ intercalation pseudocapacitance, Nat. Mater. 12 (6) (2013) 518–522.

[51] B.-A. Mei, L. Pilon, Three-dimensional cyclic voltammetry simulations of EDLC electrodes made of ordered carbon spheres, Electrochim. Acta 255 (2017) 168–178.

[52] Q. Liao, N. Li, H. Cui, C. Wang, Vertically-aligned graphene@MnO nanosheets as binder-free high-performance electrochemical pseudocapacitor electrodes, J. Mater. Chem. 1 (44) (2013) 13715–13720.

[53] S.Y. Lin, X. Zhang, Two-dimensional titanium carbide electrode with large mass loading for supercapacitor, J. Power Sources 294 (2015) 354–359.

[54] S. Lee, Y.W. Lee, D.H. Kwak, M.C. Kim, J.Y. Lee, D.M. Kim, K.W. Park, Improved pseudocapacitive performance of well-defined WO_{3-x} nanoplates, Ceram. Int. 41 (3) (2015) 4989–4995.

[55] H. Wang, L. Pilon, Physical interpretation of cyclic voltammetry for measuring electric double layer capacitances, Electrochim. Acta 64 (2012) 130–139.